Effects of strain on the stability of tetragonal ZrO_{2}

Min-Hua Chen, John C. Thomas, Anirudh Raju Natarajan, and Anton Van der Ven

Phys. Rev. B **94**, 054108 — Published 12 August 2016

DOI: 10.1103/PhysRevB.94.054108

Effects of Strain on the Stability of Tetragonal ZrO_2

Min-Hua Chen, John C. Thomas, Anirudh Raju Natarajan, and Anton Van der Ven*
Materials Department, University of California, Santa Barbara, California 93106, USA

The tetragonal form of ZrO_2 is used in a wide range of technologies. In this study, we systematically explore the effect of strain on the relative stability of symmetrically equivalent tetragonal variants of ZrO_2 using first-principles density functional theory. We focus in particular on the role that strain plays in altering metastability and causing dynamical instabilities as these properties affect the mechanisms of ferroelastic switching. We also discover the emergence of a dynamical instability in tetragonal ZrO_2 at its high temperature equilibrium volume. This indicates that the high temperature thermodynamic properties of tetragonal ZrO_2 have important anharmonic vibrational contributions that cannot be captured with the quasi-harmonic approximation. Finally, we determine that the instability of tetragonal ZrO_2 at large volumes leads to a new orthorhombic phase having a $P2_12_12_1$ space group.

I. INTRODUCTION

Zirconia (ZrO_2) and its alloys are used in a wide variety of applications. As a pure oxide it has much in common with HfO_2 and can serve as a high-k dielectric material in dynamic random access memory devices (DRAM)[1,2]. When alloyed with Y_2O_3, the resulting yttria-stabilized zirconia exhibits high oxygen conductivities making it an ideal solid electrolyte in oxygen fuel cells[3,4]. Yttria-stabilized zirconia is also used as a thermal barrier coating on jet engine turbine blades due in part to its low thermal conductivity and high toughness[5–8].

ZrO_2 is one of the many oxides that can form in the Zr-O binary[9–13], and can exist in one of three polymorphs under normal pressures depending on its temperature[14]. As a bulk phase, ZrO_2 is stable in a monoclinic crystal structure at low temperature, transforming to a tetragonal form above 1478 K[9]. At temperatures above 2500 K ZrO_2 adopts cubic symmetry[9,10,15]. Several orthorhombic polymorphs become stable at high pressures[16–18].

It is well known that cubic ZrO_2 is dynamically unstable at zero Kelvin with respect to a cooperative oxygen shuffle that takes it to the tetragonal form[19–24]. The emergence of cubic ZrO_2 at high temperatures has been attributed to large anharmonic vibrational fluctuations that on average impart the crystal with cubic symmetry[21,25]. In constrast, various approximations to density functional theory (DFT) predict lower-temperature tetragonal and monoclinic variants of ZrO_2 to be dynamically stable at their zero Kelvin equilibrium volumes[22–24].

Tetragonal ZrO_2 is especially important from a technological perspective. ZrO_2 adopts the tetragonal form when grown as a thin film for dielectric applications, maintaining tetragonal symmetry down to room temperature[26–28]. In thermal barrier coatings, the twinned microstructures of tetragonal ZrO_2 are exploited to increase toughness as the growth of favorably aligned tetragonal domains, mediated by twin boundary motion, can relieve stresses at crack tips[29,30].

Strain plays an important role in many applications where tetragonal ZrO_2 and its alloys are used. Epitaxial films are invariably subjected to anisotropic strain boundary conditions. The complex twinned and partially transformed microstructures of ZrO_2 in high temperature applications also exhibit strong variations in local strain. Large strains are present along coherent twin boundaries separating differently oriented tetragonal variants of ZrO_2. The effect of strain on the relative stability of the various polymorphs of ZrO_2 remains mostly unexplored and poorly understood.

Here we investigate the coupling between strain and oxygen-shuffle degrees of freedom in tetragonal ZrO_2. This coupling determines the mechanisms of ferroelastic switching in twinned microstructures of tetragonal ZrO_2. We introduce shuffle order parameters that conveniently describe all symmetrically equivalent tetragonal variants in terms of a minimal set of variables. Using density functional theory, we calculate the energy as a function of strain and shuffle order parameters and construct a phase diagram that maps phase stability and the onset of dynamical instabilities as a function of deviatoric strain. We also show that tetragonal ZrO_2 becomes dynamically unstable at zero Kelvin at volumes typical of its high-temperature equilibrium volume. The unstable phonon modes take tetragonal ZrO_2 to an orthorhombic phase that has not been reported previously. The emergence of dynamical instability with increasing volume has important implications for the applicability of the quasi-harmonic approximation and raises fundamental questions about the nature of thermodynamic and mechanical properties in tetragonal ZrO_2 at high temperature.

II. METHODOLOGY

Energies were calculated with the PBE parameterization[31] of the generalized gradient approximation to density functional theory as implemented in the Vienna Ab Initio Simulation Package (VASP)[32,33]. Projector augmented wave[33,34] pseudopotentials with valence-electron configurations of $4s^2, 4p^6, 5s^1, 4d^3$ and $2s^2, 2p^4$ for Zr and O, respectively, were used. The

plane wave basis energy cutoff was set to 600 eV. A $7 \times 7 \times 7$ Monkhorst-Pack k-point mesh[35] was used for the 12-atom conventional cells of ZrO_2.

The calculated conventional cubic ZrO_2 lattice parameter was $a = 5.14$ Å. The calculated lattice parameters for tetragonal ZrO_2 were $a = 5.15$ and $c = 5.30$ Å. Previously calculated lattice parameters for the cubic phase have ranges between 5.034 - 5.151 Å[22,23,25,36]. Calculated tetragonal lattice parameters vary between $a = 5.029 - 5.161$ Å and $c = 5.100 - 5.383$ Å[22,23,25,36]. The variation in calculated lattice parameters can likely be attributed to a variety of pseudopotentials being used. Experimental lattice parameters have been reported to be $a = 5.090$ Å for the cubic phase and $a = 5.050, c = 5.182$ for the tetragonal phase[37].

Phonon dispersion curves for cubic and tetragonal ZrO_2 were calculated using a finite-difference approach with the PBEsol parameterization[38]. The forces arising from single-atom finite displacements were calculated with VASP. The forces at surrounding ions are linearly related to the displacement via the interatomic force constants, which were obtained from a least-squares fit to the calculations. These force constants are used to calculate the dynamical matrix. DFT calculations for the cubic ZrO_2 dispersion curve utilized 0.03-Å displacements in a $3 \times 3 \times 3$ supercell of the primitive cell and a $3 \times 3 \times 3$ Monkhorst-Pack k-point mesh. The VASP implementation[39] of the linear response approximation[40] was used to calculate the Born effective charges and dielectric tensors used in the non-analytical correction to the dynamical matrix. The corrections accounting for long-range dipole-dipole interactions were calculated using the interpolation scheme by Parlinski et al[41].

For tetragonal ZrO_2, harmonic phonon calculations were performed at volumes ranging between -2% to $+10\%$ at increments of $+2\%$. The c/a ratio of the primitive cells was optimized manually at each volume, while allowing the ions to relax. A $15 \times 15 \times 10$ Monkhorst-Pack mesh was used for tetragonal ZrO_2. Perturbations of 0.037 and 0.048$\mathring{A}$ were imposed on the Zr and O atoms, respectively, to extract force constants in a $3 \times 3 \times 2$ supercell of the 6-atom tetragonal unit cell using a $5 \times 5 \times 5$ Monkhorst-Pack k-point mesh.

III. RESULTS

The crystal structures of the cubic, tetragonal and monoclinic polymorphs of ZrO_2 are shown in Figure 1. The Zr atoms in cubic ZrO_2 form a FCC sublattice while oxygen fills the tetrahedrally coordinated interstitial sites, which form a simple-cubic sublattice (Figure 1a). Both tetragonal and monoclinic ZrO_2 can be derived from cubic ZrO_2 by the combined application of lattice strains and internal atomic shuffles. We first focus on the internal shuffles that connect cubic and tetragonal ZrO_2. This is conveniently achieved with symmetry-adapted order parameters expressed in terms of phonon mode amplitudes. We then explore pathways that connect symmetrically equivalent tetragonal variants with each other and the cubic form and determine the role of strain in altering relative stabilities and causing dynamical instabilities.

A. Shuffle order parameters

1. *Cubic to tetragonal atomic shuffles*

Figure 2 shows the calculated phonon dispersion curves for cubic ZrO_2 along high-symmetry directions in the reciprocal lattice of the primitive unit cell of cubic ZrO_2. The dispersion curves incorporate contributions from long-range dipole-dipole interactions, which leads to the splitting of the longitudinal- and transverse-optical modes in the vicinity of Γ[42]. Consistent with past group theoretical[19] and first-principles[20,43] lattice dynamical studies, the cubic form of ZrO_2 is predicted to be dynamically unstable. This is manifested by the imaginary frequencies (represented in Figure 2 as negative frequencies) in the calculated dispersion curves at the X wave vector.

There are three symmetrically equivalent X points in the Brillouin zone of cubic ZrO_2, excluding translationally equivalent points. The 12-atom cubic unit cell shown in Figure 1a accommodates all phonon modes at the three symmetrically equivalent X points. The unstable phonon modes at each X point correspond to longitudinal shuffles of oxygen atoms along the cubic axes. The unstable phonon mode leading to oxygen shuffles along the z-axis, for example, is shown in Figure 1b. It can be described as an up and down shuffle of oxygen residing in alternating (110) planes of the cubic unit cell. We will refer to this shuffle as the $\hat{z}$ shuffle. Symmetrically equivalent oxygen shuffles can occur along the [100] direction and along the [010] direction. We will refer to these shuffles as $\hat{x}$ and $\hat{y}$ shuffles, respectively.

Displacements along the unstable mode at each X point break the cubic symmetry and, when coupled with lattice strains, connect the cubic and tetragonal forms of ZrO_2[19,20,43]. The amplitudes of the unstable phonon modes at X can therefore serve as order parameters describing the group/subgroup relationship between cubic and tetragonal ZrO_2.[21] Following Fabris et al[21], we denote the amplitudes for the $\hat{x}$, $\hat{y}$ and $\hat{z}$ shuffles with δ_x, δ_y and δ_z respectively. Here we scale the amplitudes such that they measure the distance in Angstroms with which any oxygen deviates from its ideal cubic position in the unstrained cubic reference crystal. Figure 3 shows the calculated energy of ZrO_2 as a function of δ_z while maintaining fixed cubic lattice vectors. Cubic ZrO_2 coincides with the origin in Figure 3 ($\delta_z = 0$). As the amplitude δ_z increases, the oxygen ions shuffle along the z axis. A negative amplitude describes a shuffle in the opposite direction along the z axis and yields a $\hat{z}$ shuffle that is equivalent to the postive amplitude $\hat{z}$ shuffle by a trans-

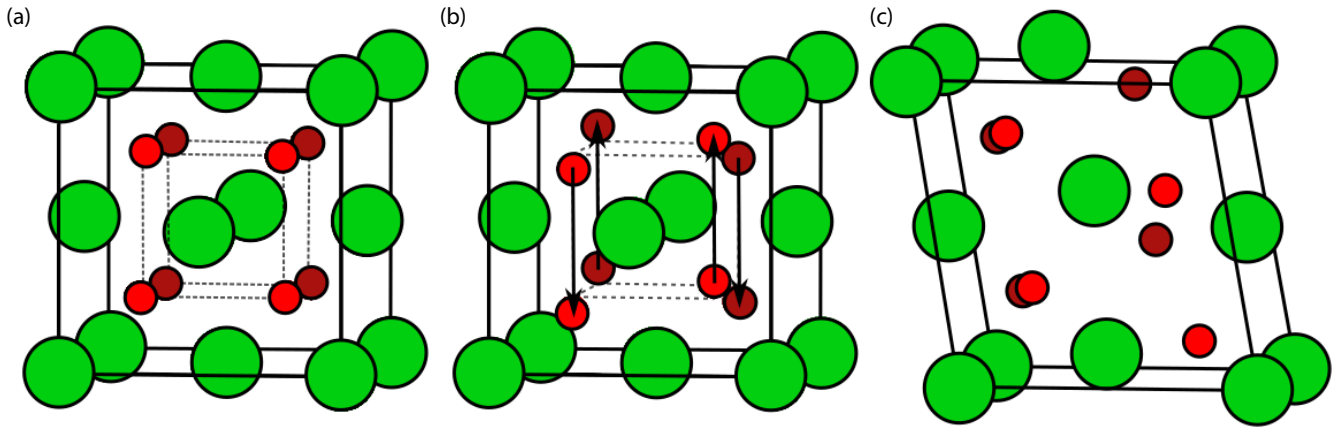

FIG. 1: ZrO_2 crystal structures. An internal oxygen shuffle applied to the cubic form (a) resulting in the tetragonal phase (b). Application of shear strain results in the monoclinic phase (c).

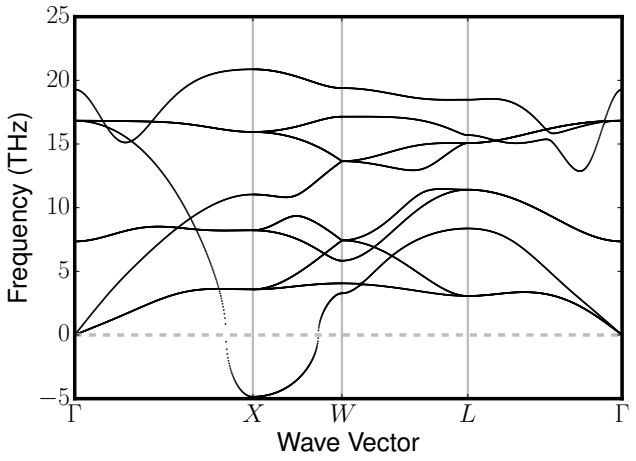

FIG. 2: Cubic ZrO_2 dispersion curve showing an instability at the Brillouin zone boundary X point.

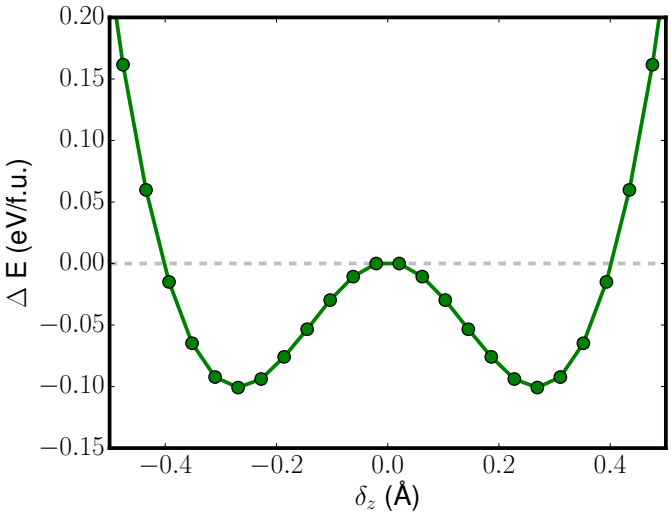

FIG. 3: Calculated energy variation with amplitude δ_z of the z tetragonal shuffle mode.

lation of the cubic ZrO_2 lattice. The energy curve in Figure 3 clearly exhibits negative curvature at $\delta_z = 0$, consistent with the imaginary vibrational frequency predicted for this phonon mode. The energy exhibits two minima at finite amplitudes of δ_z corresponding to oxygen displacements of approximately 0.27 Å. Due to the cubic symmetry of the unit cell, identical energy curves exist as a function of amplitudes δ_x and δ_y for $\hat{x}$ and $\hat{y}$ tetragonal shuffles. These results are qualitatively consistent with the first-principles calculations of Fabris et al[21] and Carbogno et al[25].

2. *Relationship between symmetrically equivalent tetragonal variants*

The cubic phase is a convenient reference state for the purpose of relating the three symmetrically equivalent tetragonal variants to each other. Symmetrically equivalent tetragonal variants of ZrO_2 are frequently observed to coexist within twinned microstructures in which coherent twin boundaries separate one tetragonal variant from the other[30,44]. Since the cubic phase is dynamically unstable with respect to the $\hat{x}$, $\hat{y}$ and $\hat{z}$ shuffles, it will also be dynamically unstable with respect to any displacement field that arises from a superposition of the three shuffles. The properties of the crystal at the macroscopic level are determined by the shuffle amplitude and orientation, but are not affected by the sign of the shuffle am-

plitude, which only distinguishes translational variants. This motivates the introduction of order parameters defined as linear combinations of the squares of the shuffle amplitudes δ_x^2, δ_y^2 and δ_z^2 according to

$$\eta_1 = \delta_x^2 + \delta_y^2 + \delta_z^2 \quad (1)$$

$$\eta_2 = \sqrt{3}(\delta_x^2 - \delta_y^2)/2 \quad (2)$$

$$\eta_3 = \left(2\delta_z^2 - \delta_y^2 - \delta_x^2\right)/2. \quad (3)$$

The definition of these order parameters is guided by how they transform under symmetry operations of the high symmetry cubic reference crystal.

The first order parameter, η_1, is invariant to any symmetry operation of the cubic reference crystal. It can be shown that η_1 is equal to the square of the distance of each oxygen from the center of its tetrahedral site, independent of displacement direction, for structures generated as a linear superposition of $\hat{x}$, $\hat{y}$ and $\hat{z}$ shuffles. The parameters η_2 and η_3 describe shuffle orientation and depend on the relative magnitudes of the shuffle amplitudes δ_x, δ_y and δ_z. Different combinations of δ_x, δ_y and δ_z shuffle amplitudes can be visualized in the η_2-η_3 plane when holding η_1 constant. By keeping η_1 constant, we restrict δ_x, δ_y and δ_z to the surface of a sphere of radius $\sqrt{\eta_1}$, as illustrated in Figure 4a. To enumerate unique combinations of δ_x, δ_y and δ_z that affect macroscopic properties, we need only consider one octant of the sphere, such as the one corresponding to only positive values of δ_x, δ_y and δ_z, highlighted in blue in Figure 4a. The other octants describe equivalent shuffle orderings, differing only by a translation vector of the cubic ZrO_2 primitive cell. Each point on an octant of the sphere can be mapped to a point in a triangle in η_2-η_3 space as illustrated in Figure 4b for the octant corresponding to positive δ_x, δ_y and δ_z. Points outside the triangle cannot be realized by physical shuffles when η_1 is held constant.

An η_2-η_3 plot at constant η_1 is roughly analogous to a pole projection of the positive octant of the sphere in Figure 4a. The corners in Figure 4b are the pure $\hat{x}$, $\hat{y}$ or $\hat{z}$ shuffles, which we denote as [100], [010] and [001]. These shuffle orderings are shown pictorially in Figure 5a-c. The mid-points between pure shuffles along the perimeter of the triangle in η_2-η_3 space are shuffles made up of equal contributions of two pure shuffles and are referred to as [011], [101] and [011] shuffles. As an example, the oxygen displacements for the [110] shuffle consisting of equal contributions of a $\hat{x}$ and $\hat{y}$ shuffle is shown in Figure 5d. The origin of the η_2-η_3 plane corresponds to an equal superposition of all three shuffles, denoted by [111]. The pattern of this shuffle is shown in Figure 5e.

3. *Energy surfaces between tetragonal variants*

The shuffle order parameters enable a visualization of pathways that connect all three symmetrically equivalent tetragonal variants to each other in a two-dimensional space. Figure 6 shows the calculated energy of cubic

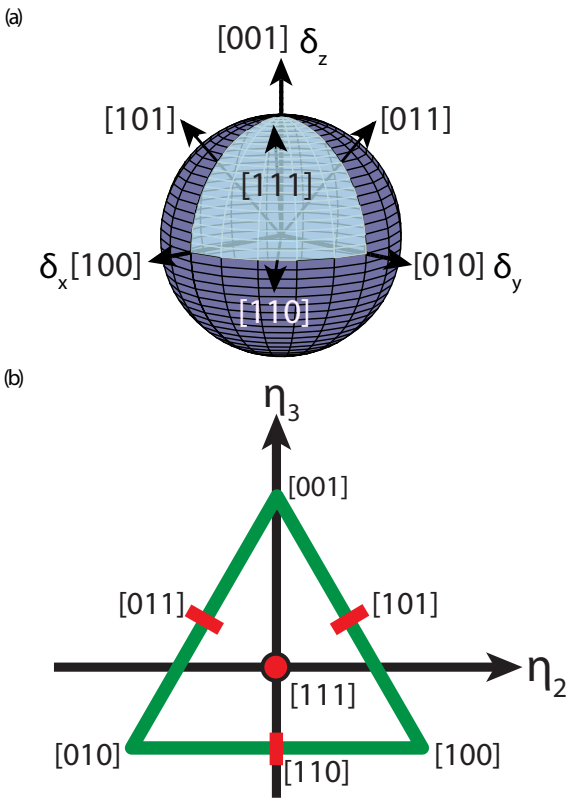

FIG. 4: (a) Sphere in $\delta_x - \delta_y - \delta_z$ space. (b) Pole map in $\eta_2 - \eta_3$ space at a fixed η_1, showing the relationship between the symmetry-adapted shuffle orientation parameters ηs to shuffle directions $[\delta_x \delta_y \delta_z]$. The green triangle bounds the region of allowed values when η_1 is held constant.

ZrO_2 as a function of η_2 and η_3 for fixed η_1. The value of η_1 was set equal to the oxygen displacement distance that minimizes the energy of the pure $\hat{z}$ shuffle (Figure 3). The energy surface in Figure 6 shows minima at the corners of the triangle in η_2-η_3 space corresponding to the pure $\hat{x}$, $\hat{y}$ and $\hat{z}$ shuffles. An equal mixture of all three shuffles at the origin of η_2-η_3 space coincides with a maximum in energy, while the minimum-energy pathway between any pair of pure shuffles passes through a shuffle consisting of an equal superposition of the end state shuffles. For example, the minimum energy path between [100] and [001] shuffles passes through [101].

The energy surface of Figure 6 is restricted to constant η_1. While the chosen value for η_1 in Figure 6 minimizes the energy of pure $\hat{x}$, $\hat{y}$ and $\hat{z}$ shuffles, it may not correspond to the optimal value when combinations of oxygen shuffles are imposed. Figure 7 shows the variation of the energy as a function of $\sqrt{\eta_1}$ for the [001], [011], and [111] shuffle orderings. The energy minimum along η_1 for the [001] pure $\hat{z}$ shuffle is lower than for the [011] and [111] shuffle orderings and occurs at a larger magnitude of η_1. The [011] shuffle ordering, consisting of an equal mixture

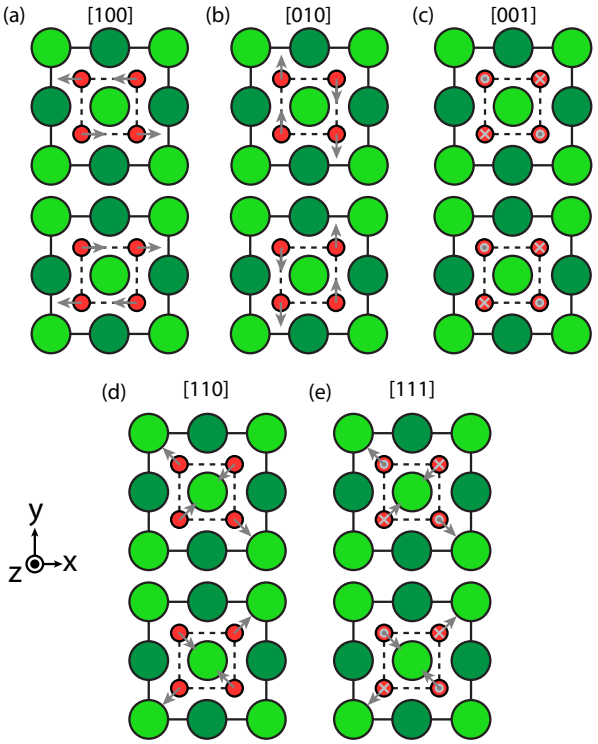

FIG. 5: Oxygen displacements associated with the (a) [100], (b) [010], (c) [001], (d) [110], and (e) [111] directions represented in the conventional cubic cell. The light green Zr atoms are in a plane above the red O atoms, while the dark green Zr atoms are in a plane below the O atoms.

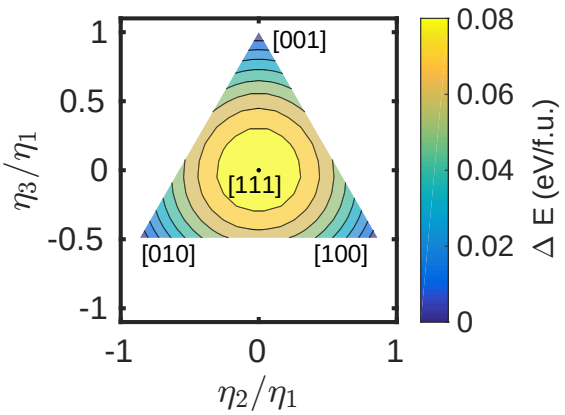

FIG. 6: A calculated energy surface of shuffles parameterized by η_2-η_3 applied to a cubic lattice. There are three equivalent energy wells due to cubic symmetry.

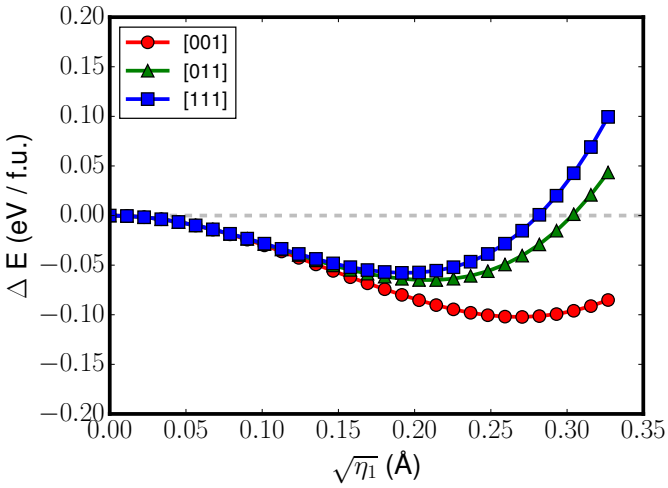

FIG. 7: Variation of $\sqrt{\eta_1}$ in the [001], [011], and [111] directions in a cubic unit cell at the equilibrium tetragonal volume.

of $\hat{y}$ and $\hat{z}$ shuffles, has a slightly higher energy minimum than [001] that occurs at a smaller magnitude of η_1. The energy minimum for the [111] shuffle ordering occurs at a value of η_1 similar to that of the [011] shuffle ordering, but is even higher in energy. Although the energy of the different shuffle orderings is sensitive to the value of η_1, the qualitative shape of the energy surface in the η_2–η_3 plane (Figure 6) is unaffected by the value of η_1. Calculated energy contours at three different η_1 values are shown in Figure S1 in Supplementary Materials. The minima remain at the vertices corresponding to the pure $\hat{x}$, $\hat{y}$, and $\hat{z}$ shuffles, independent of whether η_1 is larger or smaller than the equilibrium η_1 value for a particular shuffle ordering.

The energy surfaces of Figure 6 and Figure 7 neglect the role of additional phonon modes that may be activated to further lower the energy of the crystal as the oxygen shuffle deviates from a pure $\hat{x}$, $\hat{y}$ or $\hat{z}$ shuffle. We explored the importance of additional phonon modes by performing nudged elastic band (NEB) calculations between a $\hat{x}$ shuffle and a $\hat{z}$ shuffle within the 12 atom cubic ZrO_2 unit cell. The minimum energy path between these two shuffles is shown by the red circles in Figure 8a. Although the NEB calculations indicate that the maximum energy along this path is dominated by a mixed [101] shuffle ordering, additional phonon modes are also activated along the path. Furthermore, η_1 does not remain constant along the path, but adopts a slightly smaller value compared to its equilibrium value in the pure $\hat{x}$ and $\hat{z}$ shuffles. This is shown in Figure 8b where the value of η_1 and the norm of the residual displacements (per atom) (after projecting out the pure $\hat{x}$ and $\hat{z}$ shuffle components) are plotted along the NEB minimum energy path. Figure S2a shows the decomposition of the NEB displacements into a contribution of solely $\hat{x}$ and $\hat{z}$ shuffles, while Figure S2b shows the residual displacements. The residual displacements cause the oxygen atoms to oscillate in unison towards each other along the y-axis, then away. This anisotropic breathing mode is not to be mistaken for the $\hat{y}$ shuffle in which the oxygens in alternating (110) planes shuffle in opposite directions. In

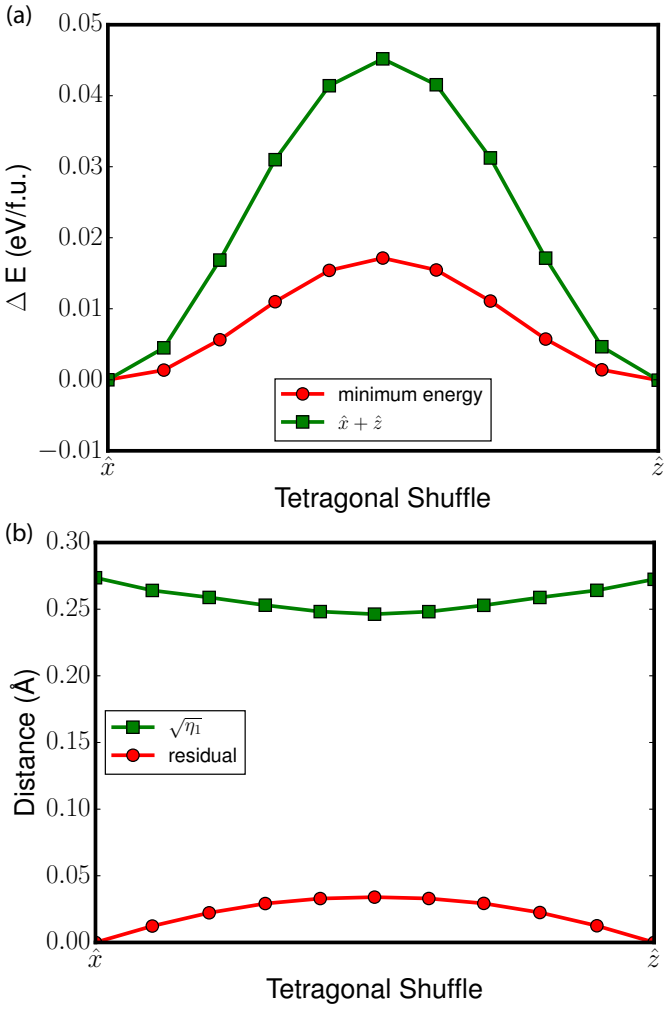

FIG. 8: (a) Comparison of energy barriers between the $\hat{x}$ and $\hat{z}$ shuffle along the path obtained from nudged elastic band (red circles) and along a path obtained involving only $\hat{x}$ and $\hat{z}$ modes (green squares). (b) The RMS shuffle magnitude, $\sqrt{\eta_1}$, along the NEB path from the $\hat{x}$ to $\hat{z}$ shuffle (green squares), as well as the RMS magnitude of residual displacements activated along the path that are not attributable to the $\hat{x}$, $\hat{y}$, and $\hat{z}$ shuffle modes (red circles).

terms of magnitudes, the NEB displacements are dominated by the $\hat{x}$ and $\hat{z}$ modes, where the maximum displacement distance is 0.27 Å. In contrast, the maximum value of the residual displacements is only 0.034 Åalong the path.

Although the residual displacements are small in magnitude, their impact on the energy barrier between the $\hat{x}$ and $\hat{z}$ shuffles is significant. The energy barrier for a pathway involving only $\hat{x}$ and $\hat{z}$ modes, shown in green squares in Figure 8a, is twice as high as that calculated along the NEB path. This suggests that Figure 6, while qualitatively capturing the variation of the energy landscape between the various shuffle modes, should be viewed as an upper-bound estimate to the true minimum-energy path.

B. Strain

While the cubic, tetragonal and monoclinic forms of ZrO_2 can be distinguished from each other on the basis of their atomic displacements within a common 12-atom unit cell, in their fully relaxed equilibrium states (at constant pressure) they also adopt different lattice vectors. Strain metrics can be used to track variations in lattice parameters and angles.

Various metrics of finite deformation, such as the Lagrange, Euler and Hencky strains, can be defined in terms of the deformation gradient tensor F. For homogeneous deformations, F relates a deformed lattice to a reference lattice according to

$$L' = FL.$$

where L refers to a 3×3 matrix containing the lattice vectors of the reference crystal as columns

$$L = \left[\vec{a} \;\; \vec{b} \;\; \vec{c} \right],$$

and where L' is defined similarly for the deformed crystal. The deformation gradient tensor can be uniquely decomposed into a product of a rotation matrix R and a symmetric stretch matrix U as

$$F = RU.$$

In this study, we use the Hencky strain metric, which is defined in terms of the stretch tensor as

$$H = \ln U.$$

Evaluation of the natural logarithm is possible using the eigendecomposition of the stretch matrix, resulting in a Hencky strain tensor of the form

$$H = \begin{pmatrix} \epsilon_{xx} & \epsilon_{xy} & \epsilon_{xz} \\ \epsilon_{yx} & \epsilon_{yy} & \epsilon_{yz} \\ \epsilon_{zx} & \epsilon_{zy} & \epsilon_{zz} \end{pmatrix}.$$

As with the symmetric stretch matrix U, the Hencky strain tensor is also symmetric.

Instead of relying on the Cartesian components of the Hencky strain tensor, it is more convenient to use strain order parameters defined as symmetry-adapted linear combinations of the components of the Hencky strain tensor. Useful strain order parameters (SOPs) can be defined when measuring strain relative to the cubic reference lattice according to

$$e_1 = \frac{\epsilon_{xx} + \epsilon_{yy} + \epsilon_{zz}}{\sqrt{3}} \tag{4}$$

$$e_2 = \frac{\epsilon_{xx} - \epsilon_{yy}}{\sqrt{2}} \tag{5}$$

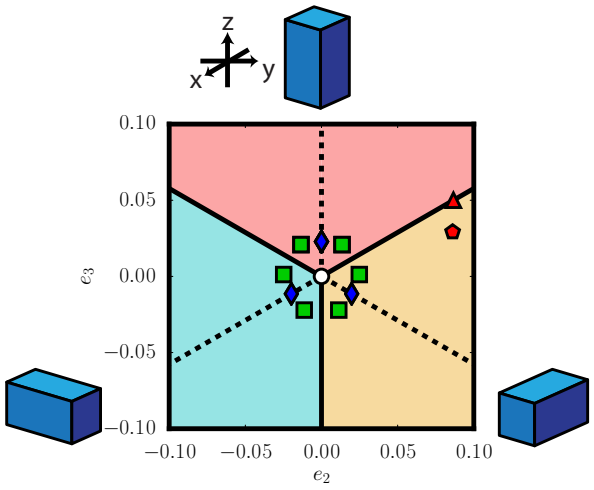

FIG. 9: An e_2-e_3 strain map showing how deviatoric strains along the dashed axes transform a cubic cell into tetragonal cells with different orientations. The pink, yellow, and blue regions show the regions where the $\hat{z}$, $\hat{x}$, and $\hat{y}$ shuffles, respectively, are energetically favorable. Cubic (white circle), tetragonal (blue diamonds), and monoclinic (green squares) strains relative to the cubic phase projected onto e_2-e_3 space.

$$e_3 = \frac{2\epsilon_{zz} - \epsilon_{xx} - \epsilon_{yy}}{\sqrt{6}} \quad (6)$$

$$e_4 = \sqrt{2}\epsilon_{yz} \quad (7)$$

$$e_5 = \sqrt{2}\epsilon_{xz} \quad (8)$$

$$e_6 = \sqrt{2}\epsilon_{xy}. \quad (9)$$

where the Cartesian axes are aligned with the cubic axes.

These SOPs are especially useful to distinguish between the cubic, tetragonal and monoclinic forms of ZrO_2 as well as all symmetrically equivalent tetragonal and monoclinic variants that can be derived from a single cubic form. The first SOP, e_1, represents a dilatational strain and is invariant to cubic symmetry operations. An advantage of the Hencky strain metric (compared to more common strain metrics such as Lagrange and Euler) is that any deformation at constant e_1 occurs at constant volume[45]. The e_2 and e_3 SOPs describe all deformations that take the reference cubic crystal at e_2=e_3=0 to tetragonal or orthorhombic symmetry. This is illustrated in Figure 9. Increasing e_3 while keeping e_2=0 results in a tetragonal distortion of the cubic reference crystal, with an elongation of the lattice vector parallel to the z axis and a contraction of the two lattice vectors in the x–y plane. Negative values of e_3 describe a contraction along the z axis coupled with an isotropic expansion in the x–y plane. Symmetrically equivalent tetragonal distortions along the x and y axis occur along the dashed lines in the e_2-e_3 plane that are rotated by 120° from the e_3 axis. The regions between dashed lines in Figure 9 describe strains that result in orthorhombic symmetry. The SOPs e_4, e_5 and e_6 describe shear strains.

The e_2 and e_3 SOPs conveniently map the three symmetrically equivalent tetragonal distortions in the same two-dimensional space. This is shown in Figure 9. The white circle at the origin represents the cubic phase, while the blue diamonds represent the three symmetrically equivalent tetragonal phases. There are twelve symmetrically equivalent monoclinic strains that can be derived from cubic ZrO_2. Each monoclinic distortion can be obtained by first straining the cubic crystal to have orthorhombic symmetry followed by a shear. The green squares in Figure 9 represent the deviatoric strains of the different monoclinic phases. Each green square in Figure 9 represents two monoclinic variants, where the two variants are further distinguished by a shear strain.

1. *Effect of e_2, e_3 Strains On Tetragonal ZrO_2*

Figure 6 shows that the $\hat{x}$, $\hat{y}$ and $\hat{z}$ shuffles all have the same energy within a cubic unit cell. Any symmetry-breaking strain of the cubic lattice, however, will break the degeneracy among the three shuffles. In this section we explore how strain modifies the relative stability among the different shuffles.

Figure 10a shows a calculated energy surface for ZrO_2 as a function of η_2 and η_3 for a unit cell distorted tetragonally along the e_3 axis, corresponding to a stretch along the z-axis and an isotropic compression in the x–y plane. The applied deviatoric strain is indicated by the blue diamond along the positive e_3 axis in Figure 9. Figure 10a shows that for this strain, the energy well for the $\hat{z}$ shuffle is a global minimum while those for the $\hat{x}$ and $\hat{y}$ shuffles are only local minima. Hence, a tetragonal elongation of the cubic axis parallel to the z axis favors a $\hat{z}$ shuffle. Nevertheless, since the energy surface also has local minima for the $\hat{x}$ and $\hat{y}$ shuffles, it is possible to realize a metastable $\hat{x}$ or $\hat{y}$ shuffle in a cell that has a tetragonal distortion along the z axis. We found that these metastable minima only exist for moderate z-oriented tetragonal strains. Above a threshold value of e_3 the two metastable minima for the $\hat{x}$ or $\hat{y}$ shuffles disappear, and only a $\hat{z}$ shuffle is stable.

Figure 10b shows an energy surface when a compressive tetragonal distortion is applied to the cubic unit cell along the y-axis (red triangle marker in Figure 9). It corresponds to a strain in e_2-e_3 space between that of a tetragonally elongated crystal along z and a tetragonally elongated crystal along x. For this strain, there are two minima coinciding with $\hat{x}$ and $\hat{z}$ shuffles. The $\hat{y}$ shuffle, however, is not stable at this strain. The tetragonal symmetry of the strain ensures that the $\hat{x}$ and $\hat{z}$ shuffles are degenerate. All degeneracies among $\hat{x}$, $\hat{y}$ and $\hat{z}$ shuffles are lifted when the symmetry is broken further by a strain that produces orthorhombic symmetry. The energy surface in Figure 10c, for example, is for an orthorhombic distortion (red pentagon marker in Figure 9) such that the lattice is longer in the z direction than the

x direction, which is in turn longer than the y direction. This energy surface shows that the well for the $\hat{z}$ shuffle is deeper than that for the $\hat{x}$ shuffle, while the $\hat{y}$ shuffle is unstable.

The effect of the deviatoric strains, e_2 and e_3, on the relative stability of $\hat{x}$, $\hat{y}$ and $\hat{z}$ shuffles is summarized in the phase diagram of Figure 11. The contour plot shows the energy of the deepest well in η_2-η_3 order-parameter space at each value of e_2 and e_3. The $\hat{z}$ shuffle is globally stable for any combinations of e_2 and e_3 strains in the red domain (at constant e_1 and zero shears). Likewise, the $\hat{y}$ ($\hat{x}$) shuffle is stable for any strain in the blue (beige) domain. The phase diagram of Figure 11 was calculated at the minimum-energy volume of tetragonal ZrO_2. The cusps at the origin and along the lines of compressive tetragonal strains (outlined in red) arise due to degeneracies among two or more wells as in the examples of Figures 6, 10a and 10b.

The dashed lines in Figure 11 signify when local minima appear or disappear. These correspond to shuffle spinodals (at zero Kelvin) where an initially metastable shuffle becomes unstable. In the center region, all three shuffles have local minima. Only one shuffle is stable for large positive tetragonal distortions, while two local minima exist for compressive tetragonal distortions. The shuffle spinodals were determined by relaxing $\hat{x}$, $\hat{y}$ and $\hat{z}$ shuffles that were slightly perturbed to determine whether they relax back to a pure shuffle, or relax to an adjacent shuffle. Additional η_2-η_3 energy landscapes, similar to those shown in Figure 10, were calculated at various strains in the e_2-e_3 and used to inform the topology of the shuffle spinodals (dashed lines) delineating the presence of various local minima. These energy landscapes are available in Figure S3 in Supplementary Materials.

2. *Minimum Energy Path Between Two Tetragonal Variants*

To consider the simultaneous effects of both strain and internal shuffles on the energetics during the $\hat{x}$ to $\hat{z}$ shuffle transition, we employ the generalized solid-state nudged elastic band (G-SSNEB) method as implemented in VASP Transition State Tools[46–48]. In contrast to the NEB method used to to calculate the energy barrier shown in Figure 8 where only internal atomic relaxations were performed within a static cubic lattice, the SS-NEB method allows for relaxations of the unit cell vectors as well. The resulting energy barrier, shown in Figure 12a, is slightly higher in energy than in Figure 8a because the end states are the true equilibrium tetragonal variants having their equilibrium lattice.

The corresponding change in strain during this $\hat{x}$ to $\hat{z}$ shuffle transition is shown in Figure 12b. The volume e_1 at the $\hat{x}$ shuffle state decreases towards the reference cubic volume before increasing again as the structure becomes increasingly $\hat{z}$ shuffled. The variation of the deviatoric strains e_2 and e_3 are projected in Figure 12c as black circles. The initial strain is in the center of the energy well belonging to the $\hat{x}$ shuffle. As the structure gradually becomes $\hat{z}$ shuffled, the deviatoric lattice strains veer towards the cubic reference at the origin. At the peak of the transformation, while the strain is closest to cubic, it remains tetragonally distorted, as represented by the black circle position on the red high-symmetry line in Figure 12c. The lattice is equally strained in both the x and z directions before fully transitioning to the z oriented tetragonal lattice at the $\hat{z}$ energy well.

3. *Effect of e_1 Strain on Tetragonal ZrO_2*

The minima in the energy contour plot of Figure 11 signify the equilibrium tetragonal deformations for each of the three symmetrically equivalent tetragonal shuffle variants at fixed e_1. Since we have used the Hencky strain, the e_2-e_3 plane describes deviatoric strains at constant volume. Changing the volume by varying e_1 will shift the position of the global minima in e_2 and e_3 space, thereby making the degree of tetragonality a function of volume. Thermodynamically, the volume can be varied by modifying the temperature. In fact, tetragonal ZrO_2 is a high-temperature phase and its equilibrium volume at elevated temperature (and zero pressure) is larger than its zero Kelvin volume as a result of thermal expansion. The equilibrium volume at a particular temperature corresponds to a minimum of the Helmholtz free energy with respect to volume. For dynamically stable phases, these free energies can be estimated with the quasi-harmonic approximation.

We explored the volume dependence of the free energy of tetragonal ZrO_2 within the quasi-harmonic approximation. Temperature dependent free energies were calculated at fixed volume within the harmonic approximation for a range of volumes between 0 to +10% of the zero-Kelvin volume. The volume dependence of the Helmholtz free energy can then be obtained by interpolation. While the dispersion curve for tetragonal ZrO_2 at its zero-Kelvin equilibrium volume, shown in Figure 13a, indicates that this phase is dynamically stable, we found that a dynamical instability emerges with increasing volume. The discontinuities in Figure 13 are a result of the directional dependence of the non-analytical correction to the dynamical matrix. The correction is necessary to account for dipole-dipole interactions in ionic crystals[41–43]. As the volume of the tetragonal unit cell increased, corresponding to an increase in e_1, the acoustic modes at the Z wave vector become increasingly unstable. The calculated phonon dispersion curve for an 8% volume increase is shown in Figure 13b. There is a clear doubly-degenerate instability at the Z wave vector, indicating that displacements along this unstable mode will lead to a lower-symmetry phase having lower energy.

The atomic displacements associated with one of the unstable modes at Z are illustrated in Figure 14a. A su-

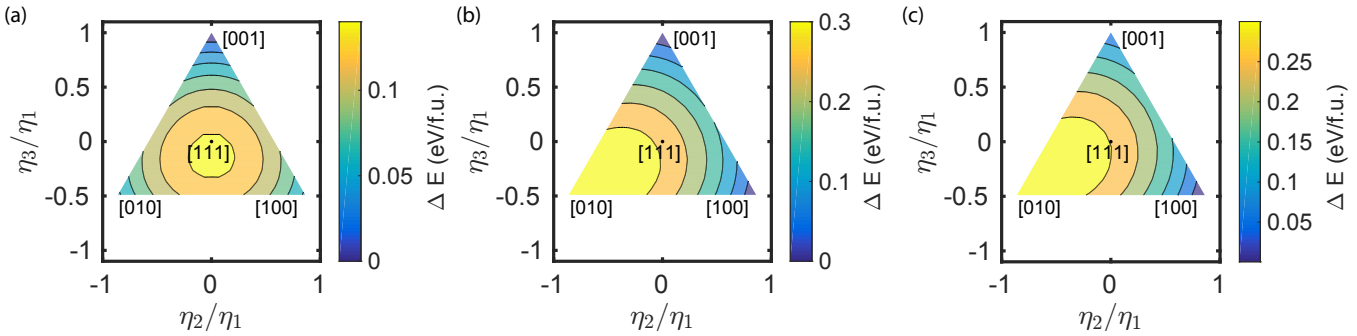

FIG. 10: η_2-η_3 energy landscapes for lattices with strains represented by the blue diamond on the e_3 axis (a), red triangle (b), and red pentagon (c) markers in the pink trisection in Figure 9. The global minimum $\hat{z}$ shuffle in (a) is 56 meV/f.u. lower in energy than the $\hat{x}$ and $\hat{y}$ shuffles.

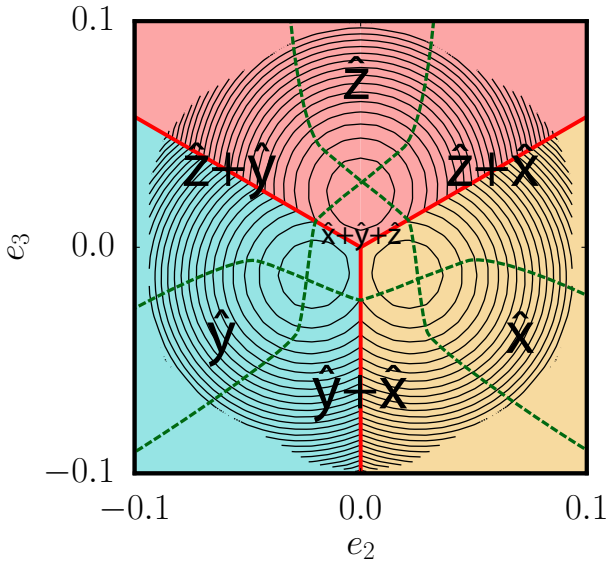

FIG. 11: Contour plot of the energy landscape for tetragonal internal shuffles at tetragonal e_1. Dashed lines show the regions of the e_2-e_3 plane where the $\hat{x}, \hat{y}, and \hat{z}$ shuffles are metastable. All three shuffles coexist in the hexagonal-like region in the center, labeled $\hat{x}+\hat{y}+\hat{z}$.

percell derived by doubling the primitive tetragonal cell along the c axis is necessary to preserve the periodicity of phonon modes at Z corresponding to $\vec{k} = (0, 0, 0.5)$. The structure in the middle of Figure 14a shows the parent tetragonal ordering, while the structures to the left and right show the displacements for positive and negative amplitudes of one of the unstable Z modes. The instabilities correspond to transverse phonon modes with displacements restricted to the a-b plane of the tetragonal super cell, which is perpendicular to the propagation direction.

The tetragonal supercell can be deconstructed as four layers of green Zr and red O atoms, as shown in Figures 14b and c. In the phonon mode shown in Figure 14b, both Zr and O atoms oscillate along the b axis, with the heavier Zr atoms displaced by larger magnitudes than the O atoms. Pairs of layers of Zr oscillate in the same direction. Every other layer of O atoms move in opposite directions from one another. Displacements of the degenerate phonon mode are shown in Figure 14c and oscillate perpendicularly along the a axis.

Figure 15 shows the calculated energy surface as a function of the amplitudes of the unstable phonon modes, ζ_1 and ζ_2. The local maximum at the origin corresponds to the ideal tetragonal structure, which serves as the zero-energy reference. There are four minima, each along either the ζ_1 or ζ_2 axis.

The impact of volumetric strain, e_1, on the stability of one of the phonon modes of Figures 14b and c is illustrated in Figure 16. For each volume, we calculated the energy as a function of amplitude ζ_1 of the phonon mode illustrated in Figure 14b. The horizontal axis in Figure 16 measures the displacement of the Zr atoms relative to their tetragonal equilibrium positions. The energies of Figure 16 were calculated at volumes ranging from +0% to +10% of the equilibrium volume. At the equilibrium volume of +0%, the energy is still fairly parabolic, but as the volume increases to +4%, the energy well flattens and becomes increasingly anharmonic. Starting at about +6%, two minima appear at positive and negative displacement amplitudes. The depth of the two energy wells increases with increasing volume. Each curve in Figure 16 was calculated at the minimum-energy c/a ratio for a given volume.

Examining the structures at the minima of the energy wells in Figure 16 reveals that they possess orthorhombic symmetry. Allowing for a full structural relaxation, we found a previously unidentified ZrO_2 orthorhomic phase, shown in Figure 17. The space group was identified as $P2_12_12_1$ (Space group #19) using the FINDSYM module of the ISOTROPY Software Suite[49]. This orthorhombic structure has lattice parameters of $a = 3.485\mathring{A}$, $b = 3.861\mathring{A}$, and $c = 10.577\mathring{A}$. There are three Wyckoff positions, which are shown in Table I. The distortions leading to the orthorhombic phase opens up tunnels run-

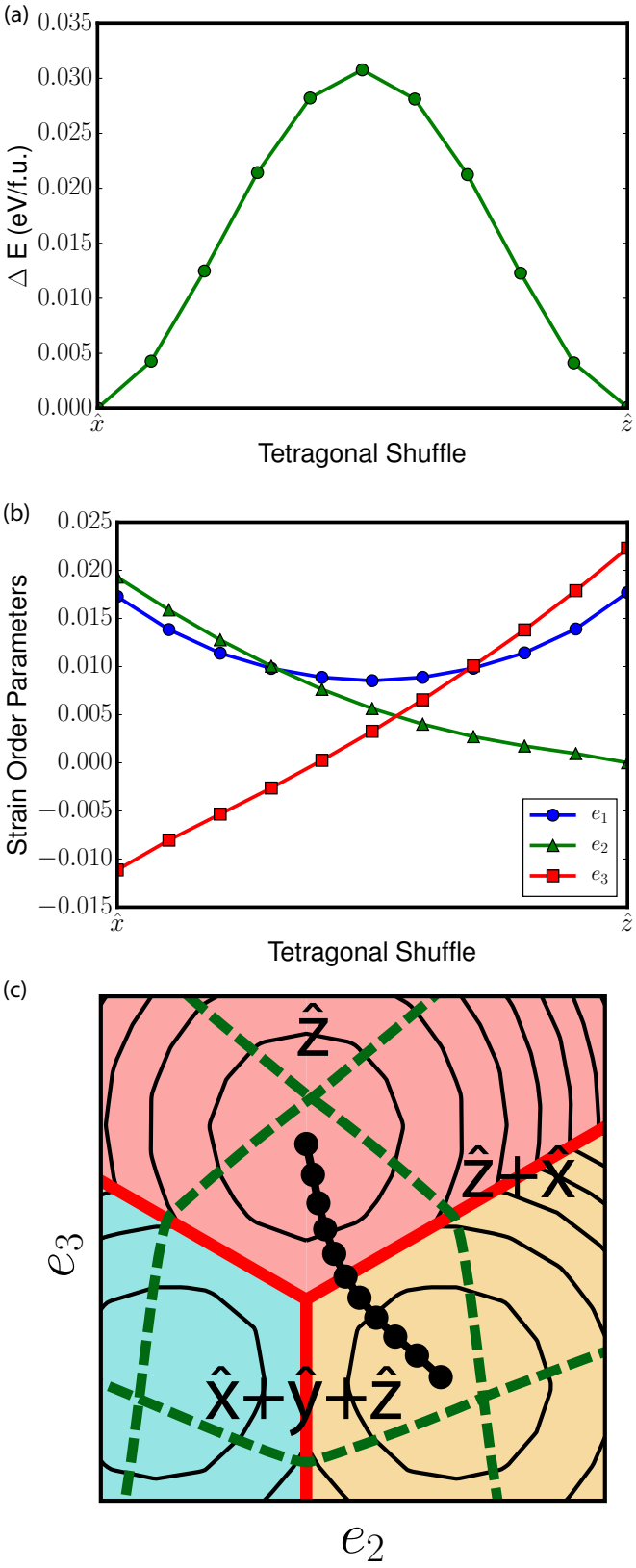

FIG. 12: (a) The energy barrier between the $\hat{x}$ and $\hat{z}$ tetragonal variants calculated allowing for structural relaxations using the solid-state nudged elastic band method. (b) The corresponding variation in strain, which is projected in e_2-e_3 space as shown in (c)

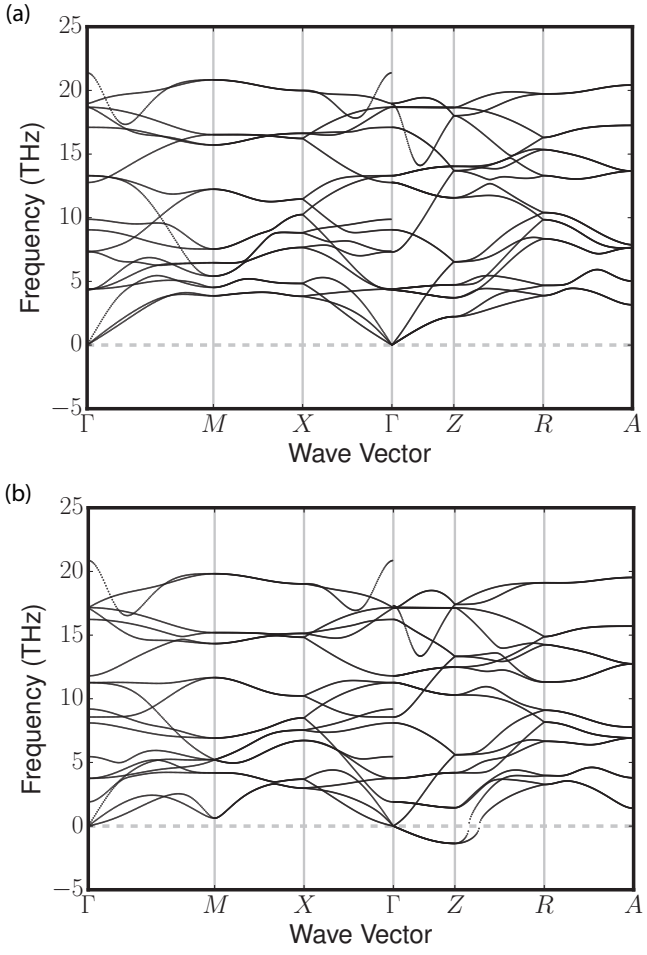

FIG. 13: Dispersion curve of tetragonal ZrO_2 (a) at equilibrium volume and (b) at +8% larger than the equilibrium volume. An instability at Z, corresponding to the point $(0, 0, 0.5)$ in the irreducible Brillouin zone, is present in (b).

TABLE I: Wyckoff positions of orthorhombic $P2_12_12_1$.

Atom	Site	Position
O	$4a$	$(0.2512, 0.4611, -0.0387)$
O	$4a$	$(0.2505, -0.3409, 0.2185)$
Zr	$4a$	$(-0.2488, 0.3312, -0.1346)$

ning parallel to the b axis.

IV. DISCUSSION

In this study, we investigated the dependence of stable and metastable tetragonal oxygen shuffles on lattice strain. This dependence is summarized in the phase diagram of Figure 11, which not only shows the globally stable shuffle orientation as a function of deviatoric strains

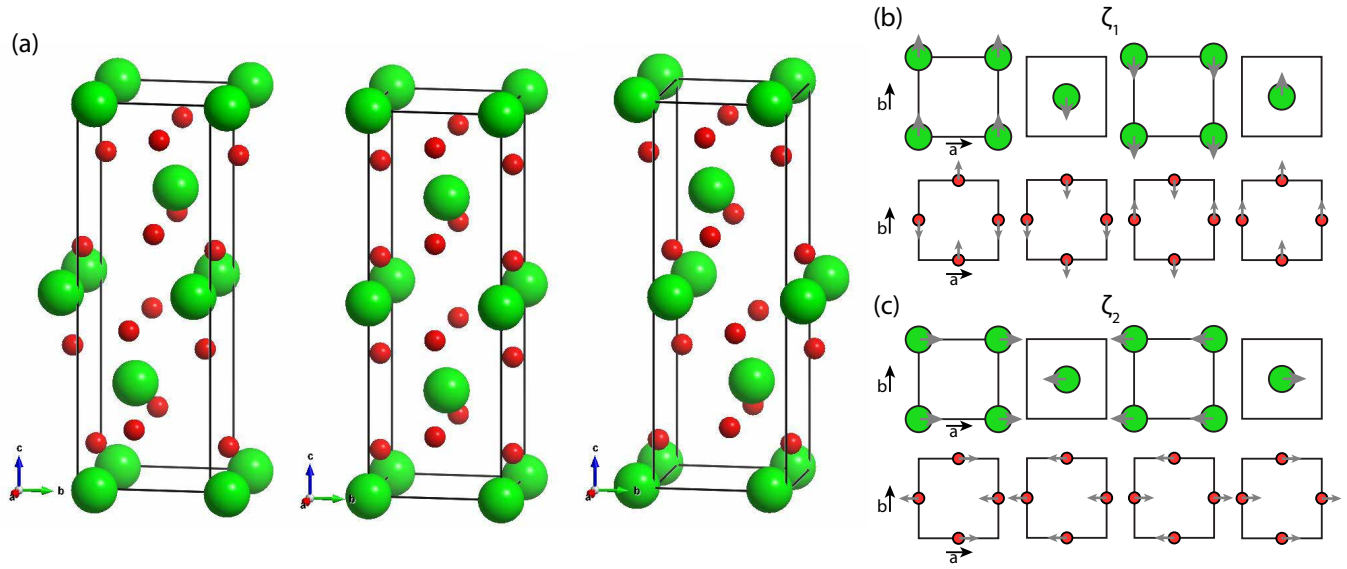

FIG. 14: (a) Illustration of the atoms displaced by the unstable phonon mode at wave vector Z in Figure 13. The image in the middle is the equilibrium tetragonal structure. Displacements of phonon modes (b) ζ_1 and (c) ζ_2 shown in the tetragonal primitive unit cell doubled in the c axis direction.

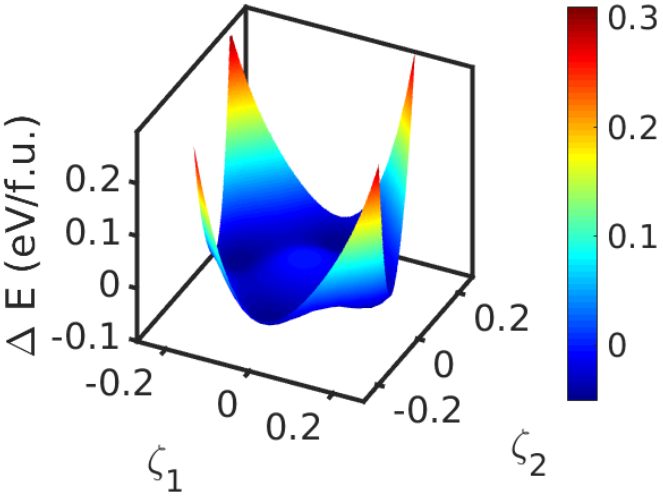

FIG. 15: Energy landscape of displacements from the two unstable phonon modes at wave vector Z.

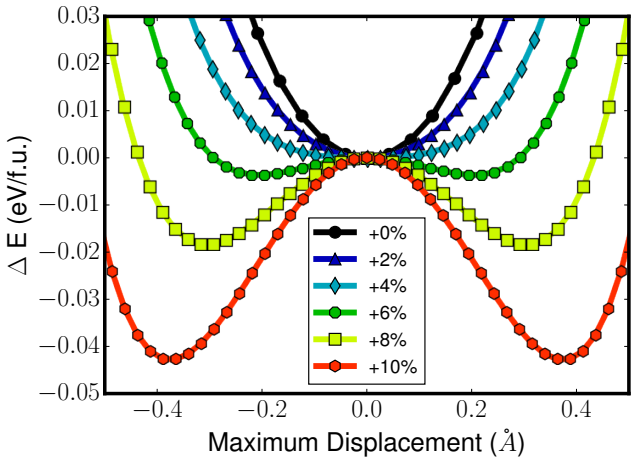

FIG. 16: Varying the magnitude of the unstable phonon mode at Z at volumes incrementally larger than the equilibrium shows that the instability appears around +3% of the equilibrium volume. The energy wells that result from the instability deepen as the volume is increased.

e_2 and e_3, but also delineates regions where more than one shuffle orientation is locally stable. The phase diagram clearly shows that there are large regions in e_2 and e_3 space where multiple shuffle orientations are locally stable. In fact, the global energy minima for the three shuffle orientations reside within a domain in e_2 and e_3 space where all three shuffle orientations are locally stable. At sufficiently low temperatures where thermal excitations are less important, it is therefore possible that a metastable $\hat{x}$ shuffle, for example, exists when the crystal is tetragonally distorted along the z axis (positive e_3 with e_2=0), where the $\hat{z}$ shuffle is globally stable.

Reorientation of the shuffle from $\hat{x}$ to $\hat{z}$ then requires a nucleation and growth mechanism due to the local stability of the metastable $\hat{x}$ orientation. The boundaries between regions where different numbers of shuffle orientations are locally stable, as delineated by the dashed lines in Figure 11, can be viewed as *shuffle spinodals*, as they are the locus of strains where a shuffle orientation that is locally stable on one side of the line becomes

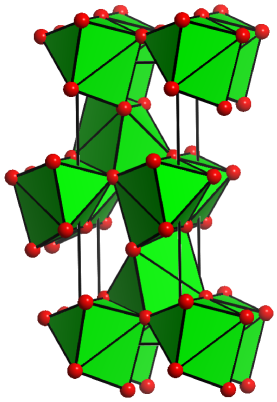

FIG. 17: The orthorhombic $P2_12_12_1$ structure resulting from the displacement mode illustrated in Figure 14.

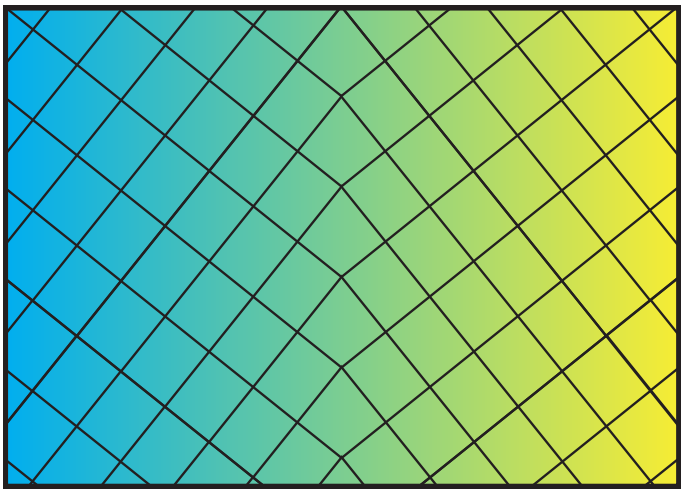

FIG. 18: A twin boundary between two tetragonal variants, which are each represented by blue and yellow regions. The gradation in color illustrates the continuous variation in strain.

dynamically unstable on the other side. A shuffle reorientation upon application of a strain that takes the ZrO_2 crystal across a shuffle spinodal will occur uniformly and without a nucleation and growth mechanism in a manner that is similar to spinodal decomposition or spinodal ordering (albeit on vibrational time scales as opposed to diffusional time scales).

The interplay between shuffle order parameters and strain, as codified in the phase diagram of Figure 11, has implications for the mechanisms of ferroelastic switching at low temperatures. Ferroelastic switching under an applied load can occur when coherent twin boundaries (Figure 18) separating domains of differently oriented tetragonal variants migrate, thereby enlarging the tetragonal domains that have their c-axis more favorably aligned with the imposed stress field at the expense of the domains that are not as favorably oriented. The equilibrium strain (relative to the cubic reference crystal) in the interior of each domain will adopt values close to their global energy minima in Figure 11. The twin boundaries and their immediate surroundings, in contrast, localize the variation in strain needed to go from one global minimum in Figure 11 to another. As a first approximation, the strain may vary continuously between two global minima as shown in Figure 12c with much of the strain variation concentrated at the twin boundary. The halfway point between the $\hat{x}$ and the $\hat{z}$ global minima, for example, corresponds to a compressed tetragonal distortion along the y-axis where the $\hat{x}$ and $\hat{z}$ shuffles are degenerate in energy. The η_2-η_3 energy surface of Figure 10b shows that at this intermediate strain, there is an additional barrier to reorient a $\hat{x}$ shuffle to a $\hat{z}$ shuffle. Hence, the twin boundary may migrate, leaving a new tetragonal strain in its wake, without a reorientation of the oxygen shuffle. This barrier to reshuffle should introduce a resistance to twin boundary migration that will be rate dependent: slow twin boundary migration gives sufficient time for nucleation and growth of reoriented shuffle domains, while fast boundary migration will trap high-energy metastable shuffle orientations. At high temperatures, thermal fluctuations are likely to modify this picture. Effective Hamiltonians can be used to predict the equivalent finite-temperature free energy surface as a function of shuffle and strain order parameters[50–53]. The dynamics of twin boundary migration can be explored at the continuum level with appropriate phase-field models that rely on homogeneous free energies as a function of shuffle and strain order parameters as well as gradient energy terms[54–58].

While it is now well established that cubic ZrO_2 is dynamically unstable with respect to a cooperative oxygen shuffle at zero Kelvin[19,20,22,24,43,59–61], this work predicts that tetragonal ZrO_2 also becomes dynamically unstable at volumes typical of its equilibrium volume at high temperature. The stability of cubic ZrO_2 at very high temperatures has been attributed to large anharmonic vibrational excitations that, on average, give the crystal cubic symmetry. Fabris *et al.*[21] applied molecular dynamics simulations to an LDA-based tight binding Hamiltonian to study the tetragonal-to-cubic transition of ZrO_2. They interpreted their results in terms of a Landau free energy description expressed as a function of shuffle amplitudes and strains. Their analysis predicted a second-order tetragonal-to-cubic transition of a displacive nature, whereby the average value of the shuffle amplitude gradually decreases to zero upon approaching the transition temperature from below. Carbogno *et al.*[25] also investigated the tetragonal and cubic forms of ZrO_2 with molecular dynamics simulations using PBEsol. They found that thermal excitations induce spontaneous switching between tetragonal shuffle orientations and concluded that the experimental cubic form of ZrO_2 exists as a thermodynamic average of all three tetragonal displacement orientations. Similar high-temperature stabilization of phases that are dynamically unstable at

zero Kelvin has been predicted for perovskites[50,62,63] and transition metal hydrides[51,52]. The presence of the instabilities in tetragonal ZrO_2 at larger volumes suggests that large anharmonic vibrational excitations, similar to those that stabilize cubic ZrO_2, are responsible for the stability of the tetragonal phase at high temperature.

The orthorhombic structure that tetragonal ZrO_2 relaxes into at large volumes where it becomes dynamically unstable has the $P2_12_12_1$ space group. This new orthorhombic structure joins a long list of known orthorhombic polymorphs, that include orthorhombic phases having $Pbc2_1$[64], $Pnma$, and $Pbca$[18] space groups. Both $Pbca$ and $Pnma$ are stable at elevated pressures, and phonon studies of these phases at ambient pressures have shown them to be dynamically stable[65]. The $Pbc2_1$ phase was first found in magnesium partially-stabilized-zirconia[64]. Figure 19 shows the calculated volume-energy relationships between all known ZrO_2 polymorphs, along with the new $P2_12_12_1$ phase, represented by a black diamond. The calculated volume-energy trend shown in Figure 19 among cubic, tetragonal, and monoclinic polymorphs is consistent with previous reports[22,36]. There is a slight volume expansion associated with the cubic-to-tetragonal transition. A larger volume expansion of approximately 5% accompanies the transition from tetragonal to monoclinic ZrO_2. The $P2_12_12_1$ phase is larger in volume than the tetragonal phase and has almost the same volume as the monoclinic phase. The $P2_12_12_1$ phase, however, is still approximately 60 meV/f.u. higher in energy than the monoclinic. There is a general trend in Zr coordination number and energy levels, where the energy increases as Zr coordination increases. The $P2_12_12_1$, $Pbca$, $Pbc2_1$, and monoclinic polymorphs have Zr atoms that are 7-fold coordinated by oxygen, and these structures are lowest in energy. The Zr atoms in the tetragonal and cubic phases are 8-fold coordinated and are both higher in energy than the seven-fold coordinated structures. $Pnma$, which is under the most compression and has 9-fold Zr coordination is highest in energy.

A consequence of the emergence of dynamical instabilities in tetragonal ZrO_2 with increasing volume is that the quasiharmonic approximation can not be applied above the volume at which the instability emerges. Rather, more elaborate and involved models accounting for the anharmonicity[50,52,66–69] of the crystal are required. Our quasi-harmonic calculations suggest that the approximation becomes invalid for tetragonal ZrO_2 above 1500K, when the predicted equilibrium volume becomes larger than the volume at which dynamical instabilities emerge. Recent work by Fultz and co-workers has also suggested the inadequacy of the quasi-harmonic approximation in capturing anharmonicity in rutile TiO_2 and monoclinic ZrO_2 at high temperatures[70,71]. Similar phonon-mode softening with increasing volume was predicted for rutile TiO_2, for example, which is not observed experimentally[70]. In our study of tetragonal ZrO_2, the volume expansion leads to an actual instability of a phonon mode that takes the tetragonal crystal to an orthorhombic form of ZrO_2. Given that the new orthorhombic phase is higher in energy than the monoclinic phase, as well as the other orthorhombic phases, it is unlikely that it will be observed experimentally. Instead the orthorhombic phase corresponds to a metastable local minimum in the energy surface of ZrO_2 as a function of vibrational degrees of freedom that can be accessed from tetragonal ZrO_2 along a dynamically unstable phonon mode at large volumes. The crystallography of the new orthorhombic phase, while likely inaccessible experimentally, is of importance in determining the nature of anharmonic vibrational fluctuations that entropically stabilize the high temperature tetragonal form of ZrO_2.

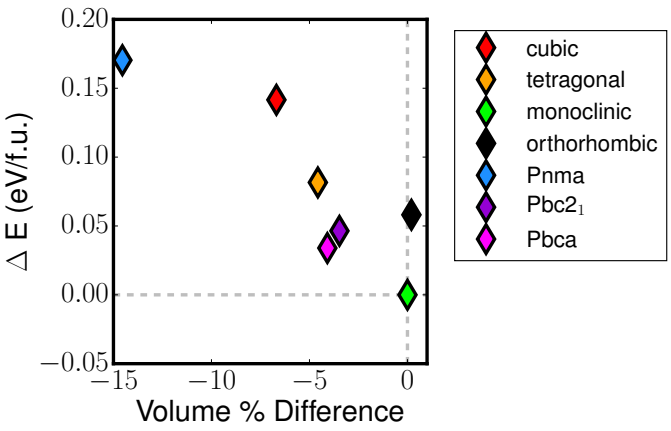

FIG. 19: Energy-volume relationships between the known ZrO_2 polymorphs relative to monoclinic ZrO_2. The black diamond marker is the newly identified orthorhombic phase with a space group of $P2_12_12_1$.

V. CONCLUSION

We studied the effect of strain on the stability of the oxygen shuffles characterizing tetragonal ZrO_2. Three symmetrically equivalent tetragonal forms of ZrO_2 can be derived from cubic ZrO_2. First-principles electronic structure calculations based on density functional theory were performed to construct a phase diagram showing the stability of the three symmetrically equivalent tetragonal variants of ZrO_2 as a function of deviatoric strains measured relative to cubic ZrO_2. The calculated phase diagram, in addition to showing global stability, also maps domains where more than one oxygen shuffle is locally stable. The prediction that several tetragonal shuffles can be locally stable at the same strain has consequences for mechanisms of ferroelastic switching. We also explored the effect of dilational strain (volume expansion) on the stability of tetragonal ZrO_2 and predict that a dynamical instability emerges at its high-temperature equilibrium volume. This result indicates that tetragonal ZrO_2 belongs to a class of phases, that includes rutile TiO_2[70] and monoclinic ZrO_2[71], in which an increase in volume leads

to large anharmonic vibrational excitations that cannot be described within the quasi-harmonic approximation.

ACKNOWLEDGMENTS

This material is based upon work supported by the National Science Foundation, Grant No. DMR-1105672. Dr. John C. Thomas was supported by the Consortium for Advanced Simulation of Light Water Reactors (http://www.casl.gov), an Energy Innovation Hub (http://www.energy.gov/hubs) for Modeling and Simulation of Nuclear Reactors under U.S. Department of Energy Contract No. DE-AC05-00OR22725. Resources of the National Energy Research Scientific Computing Center, a DOE Office of Science User Facility supported by the Office of Science of the U.S. Department of Energy under Contract No. DE-AC02-05CH11231 are gratefully acknowledged, in addition to support from the Center for Scientific Computing at the CNSI and MRL: an NSF MRSEC (DMR-1121053) and NSF CNS-0960316. Crystal structure images were generated using VESTA[72].

* avdv@engineering.ucsb.edu

[1] M. Balog, M. Schieber, M. Michman, and S. Patai, Journal of The Electrochemical Society **126**, 1203 (1979).
[2] C. S. Hwang and H. J. Kim, Journal of Materials Research **8**, 1361 (1993).
[3] J. M. Dixon, L. D. LaGrange, U. Merten, C. F. Miller, and J. T. Porter, Journal of The Electrochemical Society **110**, 276 (1963).
[4] J. W. Fergus, Journal of Power Sources **162**, 30 (2006).
[5] D. Clarke and C. Levi, Annual Review of Materials Research **33**, 383 (2003).
[6] R. Mvrel, J.-C. Laizet, A. Azzopardi, B. Leclercq, M. Poulain, O. Lavigne, and D. Demange, Journal of the European Ceramic Society **24**, 3081 (2004).
[7] O. Fabrichnaya, M. Wang, Ch.and Zinkevich, F. Aldinger, and C. G. Levi, Journal of Phase Equilibria and Diffusion **26**, 591 (2005).
[8] A. Evans, D. Clarke, and C. Levi, Journal of the European Ceramic Society **28**, 1405 (2008), developments in Ceramic Science and Engineering: the last 50 years. A meeting in celebration of Professor Sir Richard Brook's 70th Birthday.
[9] J. Abriata, J. Garcs, and R. Versaci, Bulletin of Alloy Phase Diagrams **7**, 116 (1986).
[10] R. Arroyave, L. Kaufman, and T. W. Eagar, Calphad **26**, 95 (2002).
[11] B. P. Burton, A. van de Walle, and H. T. Stokes, Journal of the Physical Society of Japan **81**, 014004 (2012).
[12] B. Puchala and A. Van der Ven, Phys. Rev. B **88**, 094108 (2013).
[13] M.-H. Chen, B. Puchala, and A. Van der Ven, Calphad **51**, 292 (2015).
[14] O. Ruff and F. Ebert, Zeitschrift fr anorganische und allgemeine Chemie **180**, 19 (1929).
[15] D. K. SMITH and C. F. CLINE, Journal of the American Ceramic Society **45**, 249 (1962).
[16] O. Ohtaka, T. Yamanaka, S. Kume, E. Ito, and A. Navrotsky, Journal of the American Ceramic Society **74**, 505 (1991).
[17] C. J. Howard, E. H. Kisi, and O. Ohtaka, Journal of the American Ceramic Society **74**, 2321 (1991).
[18] J. E. Jaffe, R. A. Bachorz, and M. Gutowski, Phys. Rev. B **72**, 144107 (2005).
[19] K. Negita, Acta Metallurgica **37**, 313 (1989).
[20] K. Parlinski, Z.-. Q. Li, and Y. Kawazoe, Phys. Rev. Lett. **78**, 4063 (1997).
[21] S. Fabris, A. T. Paxton, and M. W. Finnis, Phys. Rev. B **63**, 094101 (2001).
[22] X. Zhao and D. Vanderbilt, Phys. Rev. B **65**, 075105 (2002).
[23] M. Sternik and K. Parlinski, The Journal of Chemical Physics **122**, 064707 (2005).
[24] A. Kuwabara, T. Tohei, T. Yamamoto, and I. Tanaka, Phys. Rev. B **71**, 064301 (2005).
[25] C. Carbogno, C. G. Levi, C. G. Van de Walle, and M. Scheffler, Phys. Rev. B **90**, 144109 (2014).
[26] H. Kim, C. O. Chui, K. C. Saraswat, and P. C. McIntyre, Applied Physics Letters **83**, 2647 (2003).
[27] H. Kim, P. C. McIntyre, and K. C. Saraswat, Journal of Materials Research **19**, 643 (2004).
[28] S. K. Kim and C. S. Hwang, Electrochemical and Solid-State Letters **11**, G9 (2008).
[29] A. V. Virkar and R. L. K. Matsumoto, Journal of the American Ceramic Society **69**, C (1986).
[30] C.-J. Chan, F. F. Lange, M. Rhle, J.-F. Jue, and A. V. Virkar, Journal of the American Ceramic Society **74**, 807 (1991).
[31] J. P. Perdew, K. Burke, and M. Ernzerhof, Phys. Rev. Lett. **77**, 3865 (1996).
[32] G. Kresse and D. Joubert, Phys. Rev. B **59**, 1758 (1999).
[33] G. Kresse and J. Furthmüller, Phys. Rev. B **54**, 11169 (1996).
[34] P. E. Blöchl, Phys. Rev. B **50**, 17953 (1994).
[35] H. J. Monkhorst and J. D. Pack, Phys. Rev. B **13**, 5188 (1976).
[36] X. Zhao, D. Ceresoli, and D. Vanderbilt, Phys. Rev. B **71**, 085107 (2005).
[37] E. V. Stefanovich, A. L. Shluger, and C. R. A. Catlow, Phys. Rev. B **49**, 11560 (1994).
[38] J. P. Perdew, A. Ruzsinszky, G. I. Csonka, O. A. Vydrov, G. E. Scuseria, L. A. Constantin, X. Zhou, and K. Burke, Phys. Rev. Lett. **100**, 136406 (2008).
[39] M. Gajdoš, K. Hummer, G. Kresse, J. Furthmüller, and F. Bechstedt, Phys. Rev. B **73**, 045112 (2006).
[40] S. Baroni, S. de Gironcoli, A. Dal Corso, and P. Giannozzi, Rev. Mod. Phys. **73**, 515 (2001).
[41] K. Parlinski, Z. Q. Li, and Y. Kawazoe, Phys. Rev. Lett. **81**, 3298 (1998).
[42] M. Born and K. Huang, *Dynamical theory of crystal lattices*, International series of monographs on physics (Clarendon Press, 1954).

[43] F. Detraux, P. Ghosez, and X. Gonze, Phys. Rev. Lett. **81**, 3297 (1998).
[44] C. Mercer, J. Williams, D. Clarke, and A. Evans, Proceedings of the Royal Society of London A: Mathematical, Physical and Engineering Sciences **463**, 1393 (2007).
[45] H. Hencky, Zeitschrift für Technische Physik **9**, 215 (1928).
[46] G. Henkelman, B. P. Uberuaga, and H. Jnsson, The Journal of Chemical Physics **113**, 9901 (2000).
[47] G. Henkelman and H. Jnsson, The Journal of Chemical Physics **113**, 9978 (2000).
[48] D. Sheppard, P. Xiao, W. Chemelewski, D. D. Johnson, and G. Henkelman, The Journal of Chemical Physics **136**, 074103 (2012).
[49] H. T. Stokes and D. M. Hatch, Journal of Applied Crystallography **38**, 237 (2005).
[50] W. Zhong, D. Vanderbilt, and K. M. Rabe, Phys. Rev. Lett. **73**, 1861 (1994).
[51] J. Bhattacharya and A. Van der Ven, Acta Materialia **56**, 4226 (2008).
[52] J. C. Thomas and A. Van der Ven, Phys. Rev. B **88**, 214111 (2013).
[53] J. C. Thomas and A. Van der Ven, Phys. Rev. B **90**, 224105 (2014).
[54] D. Fan and L.-Q. Chen, Journal of the American Ceramic Society **78**, 769 (1995).
[55] Y. Wang and J. Li, Acta Materialia **58**, 1212 (2010).
[56] L.-Q. Chen, Annual Review of Materials Research **32**, 113 (2002).
[57] S. Rudraraju, A. Van der Ven, and K. Garikipati, Computer Methods in Applied Mechanics and Engineering **278**, 705 (2014).
[58] S. Rudraraju, A. Van der Ven, and K. Garikipati, Npj Computational Materials **2**, 16012 EP (2016), article.
[59] G. Jomard, T. Petit, A. Pasturel, L. Magaud, G. Kresse, and J. Hafner, Phys. Rev. B **59**, 4044 (1999).
[60] S. Fabris, A. T. Paxton, and M. W. Finnis, Phys. Rev. B **61**, 6617 (2000).
[61] A. Eichler, Phys. Rev. B **64**, 174103 (2001).
[62] U. V. W. K. M. Rabe, Philosophical Transactions: Mathematical, Physical and Engineering Sciences **354**, 2897 (1996).
[63] J. Íñiguez and D. Vanderbilt, Phys. Rev. Lett. **89**, 115503 (2002).
[64] E. H. Kisi, C. J. Howard, and R. J. Hill, Journal of the American Ceramic Society **72**, 1757 (1989).
[65] G. Fadda, G. Zanzotto, and L. Colombo, Phys. Rev. B **82**, 064105 (2010).
[66] O. Hellman, I. A. Abrikosov, and S. I. Simak, Phys. Rev. B **84**, 180301 (2011).
[67] B. Monserrat, N. D. Drummond, and R. J. Needs, Phys. Rev. B **87**, 144302 (2013).
[68] X. Ai, Y. Chen, and C. A. Marianetti, Phys. Rev. B **90**, 014308 (2014).
[69] F. Zhou, W. Nielson, Y. Xia, and V. Ozoliņš, Phys. Rev. Lett. **113**, 185501 (2014).
[70] T. Lan, C. W. Li, O. Hellman, D. S. Kim, J. A. Muñoz, H. Smith, D. L. Abernathy, and B. Fultz, Phys. Rev. B **92**, 054304 (2015).
[71] C. W. Li, H. L. Smith, T. Lan, J. L. Niedziela, J. A. Muñoz, J. B. Keith, L. Mauger, D. L. Abernathy, and B. Fultz, Phys. Rev. B **91**, 144302 (2015).
[72] K. Momma and F. Izumi, Journal of Applied Crystallography **41**, 653 (2008).